# Acquiring seismic rotations with magnetometers

*Ohad Barak, Kerry Key, Steven Constable, and Shuki Ronen*

## ABSTRACT

Induction-coil magnetometers generate current when they are rotated within the Earth's magnetic field. The current is proportional to the amount of rotation. We show how to obtain seismic rotations from magnetometer recordings. To validate the method, we performed a seismic survey where both magnetometers and inertial rotation sensors were used to record waves generated by an active source. Our results indicate that seismic rotations can be derived from induction-coil magnetometers if the ambient magnetic noise level is low and if the rotation axis is not coincident with the Earth's ambient magnetic field's direction.

## INTRODUCTION

Rigid bodies in a three dimensional world have six degrees of freedom: three components of translation and three components of rotation, as illustrated in Figure 1.

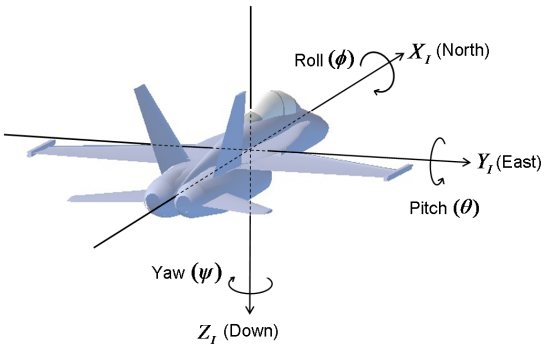


Figure 1: Sketch of the six degrees of freedom of a rigid body in a 3D world. [**NR**]

The time derivatives of translations are the particle velocities and the rotations are the pitch, roll and yaw, as shown in the following table:

| Axis | Particle velocity | | Rotation rate | |
|---|---|---|---|---|
| Z | Vertical | $v_z$ | Yaw | $r_z$ |
| X | Radial | $v_x$ | Roll | $r_x$ |
| Y | Transverse | $v_y$ | Pitch | $r_y$ |

where $v_i$ are particle velocities along the $i$ axis, and $r_i$ are rotation rates around the $i$ axis.

Vassallo et al. (2012) use hydrophones together with pressure gradient sensors in marine streamer acquisition to interpolate the pressure wavefield in the crossline direction between streamer cables. Similarly, the rotational components can be used to interpolate vertical geophone data (Muyzert et al., 2012), and spatial aliasing of high-wavenumber arrivals can thus be mitigated. Edme et al. (2014) treat rotational data as a noise model for ground-roll, and use adaptive subtraction in order to remove ground roll from the vertical component of geophone land data. Barak and Ronen (2016) show that rotation data are extra information and are independent of geophone data. They use rotational data in conjunction with translational geophone data to identify and separate wave modes on land using singular-value decomposition polarization analysis in the complex wavelet domain. Pillet et al. (2009) discuss the effect of seismic rotations on geophone recordings for the case of near-field earthquakes, and conclude that a direct recording of rotations is required in order to correct the geophone measurements for tilting generated by the seismic waves. The 2009 special issue of the Bulletin of the Seismological Society of America (Lee et al., 2009) discuss multiple applications for seismic rotation data, of particular interest to the earthquake seismology and earthquake engineering community.

## Magnetometers as rotation sensors

One way of recording seismic rotations in field exploration surveys is with an inertial rotation sensor, an example of which is shown in Figure 2. However, few of these field-deployable sensors exist, and as of yet there are no industry-grade solutions for recording rotational motion on the scale required by modern exploration seismology acquisition.

The objective of this paper is to show how rotation data can be derived from Induction-Coil Magnetometer (ICM) recordings. This concept was explored previously in Kappler et al. (2006) using earthquake data recorded by USGS permanent land stations in California. We expand on this concept and conduct a seismic field survey using both rotations sensors and ICMs, to validate if and how ICMs may be used as seismic rotation sensors.

ICMs are currently being used in large-scale magnetotelluric and controlled-source electromagnetic surveys, and are field deployable in both land and marine environments. Therefore, the possibility of deriving seismic rotations from magnetometers is compelling, as this acquisition technology is robust and has already seen academic and commercial use.

ICMs (Figure 3) operate according to Faraday's law. Copper wire is wound around a magnetically permeable core. When a change in the magnetic flux perpendicular to the coil's cross-section occurs, a current is induced in the wires.

We explain the connection between magnetic flux changes and seismic rotations as follows: Assume three orthogonal ICMs coupled to the ground, and rotating with the ground as a result of a seismic wave generating a rotational deformation of the

medium. The Earth's magnetic field, however, does not rotate and is effectively constant in direction and in amplitude for the period of the seismic wave. The ground rotation therefore manifests itself as a change in the projection of the Earth's magnetic field on the orthogonal ICM components. An illustration of this is shown in Figure 4.

The change in projection of the Earth's magnetic field on the ICM components results in a change of flux through the coils, and generates a current. After designature of the ICM, and taking into account the local magnetic field at the point of measurement, we can translate the ICM recording of magnetic flux deviations in Teslas to rotations in radians.

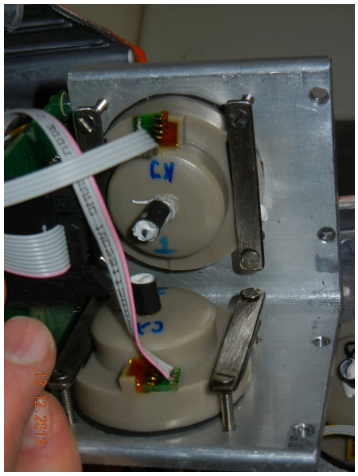

Figure 2: An inertial rotation sensor. The ring structure is filled with an electrolytic fluid, which generates a current when the sensor rotates around the axis perpendicular to the ring. The amount of current is proportional to the rotation rate. Each sensor has three perpendicular rings, and can therefore record 3-component ground rotations. [**NR**]

Figure 3: Induction-Coil Magnetometers, built by the Scripps Institute Marine EM Lab. Coils of copper wire are wound around a magnetically permeable core. A current is induced in the wire when the magnetic flux perpendicular to the coil's cross section changes. [**NR**]

## Rotations are medium strains

Hooke's law of linear elasticity states that the stress $\sigma_{ij}$ and strain $\epsilon_{ij}$ tensors are related by the fourth-order stiffness tensor $C_{ijkl}$ as

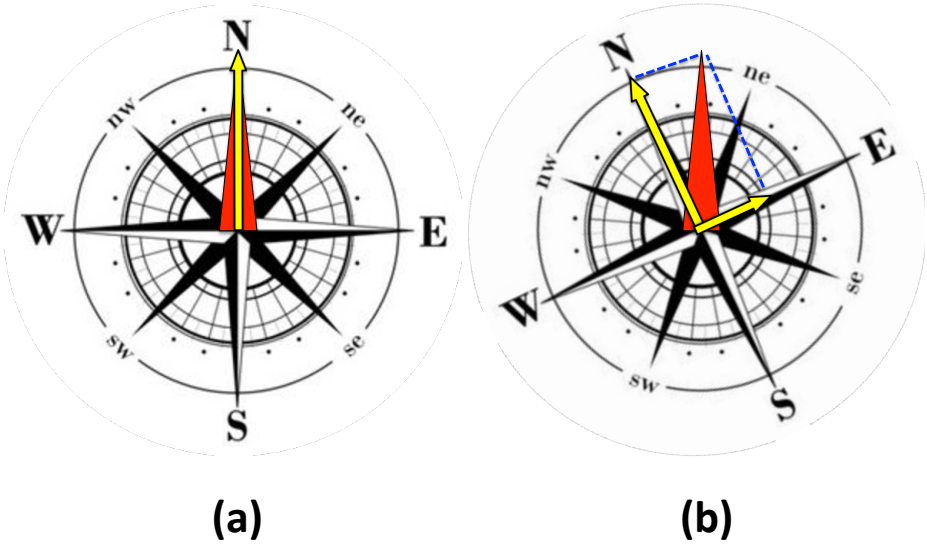


Figure 4: Illustration of how ground rotation is recorded on the magnetic field sensor as represented by the compass, which is coupled to the ground. (a) Before ground rotation, the magnetic field (red) is recorded only by the North component (yellow). (b) During ground rotation, the magnetic field (red) does not change, but its projection on the North and East components (yellow) changes. We can calculate the amount of rotation from the change in projection. Note that translations of the ground will not result in a change of the projection of the magnetic field on the magnetic components. [**NR**]

$$\sigma_{ij} = -\sum_{k=1}^{3}\sum_{l=1}^{3} C_{ijkl}\epsilon_{kl}, \tag{1}$$

where the strains are the spatial derivatives of particle displacements $\vec{u}$: $\epsilon_{ij} = \partial_j u_i$.

Geophones record particle velocities, the time-derivative of particle displacements: $\vec{v}$.

A hydrophone records the volumetric strain, which is the trace of the strain tensor. It is proportional to the divergence of the translational wavefield: $P = \kappa\partial_i u_i = \kappa\left(\nabla\cdot\vec{u}\right)$, where $\kappa$ is the bulk modulus of the water to which the hydrophones are coupled.

Rigid body rotations, which do not enter into Hooke's law, are the anti-symmetric part of the strain tensor (Cochard et al., 2006):

$$\Omega_{ij} = \frac{1}{2}\left(\partial_j u_i - \partial_i u_j\right). \tag{2}$$

Rotations are therefore a measurement of the curl of the particle displacement wavefield: $\vec{R} = \frac{1}{2}(\nabla\times\vec{u})$.

Since strains are spatial derivatives of displacements, we may conclude that geophones do not record strains, as they measure medium displacements and not the spatial derivatives of those displacements. In other words, just as we may not expect to record pressure with geophones, we similarly cannot expect them to record rotations.

However, it is possible to estimate rotations by differencing closely-spaced geophones. In Hooke's law, the stress-displacement relation for tangential stresses reads:

$$\sigma_{ij} = \mu\left(\partial_j u_i + \partial_i u_j\right), \tag{3}$$

where $\sigma_{ij}$ are the tangential stresses, $u_i$ are particle displacements and $\mu$ is the shear modulus.

At a free surface, or when going from a medium with shear strength to one without shear strength (such as the ocean-bottom interface), the tangential stresses $\sigma_{ij}$ are zero. Therefore, assuming we have receivers laid out on a flat free surface, we have

$$\begin{aligned} \partial_z u_y &= -\partial_y u_z, \\ \partial_z u_x &= -\partial_x u_z, \end{aligned} \tag{4}$$

meaning that the vertical derivative of the horizontal displacement component is equal to the horizontal derivative of the vertical displacement component.

Rotation is defined as the curl of the wavefield. Since geophones record the time-derivative of displacement (particle velocity), we use the time-derivative of rotation, or rotation rate:

$$\vec{r} = \frac{1}{2}(\nabla \times \vec{v}) = \frac{1}{2}\left(\hat{X}\left(\partial_y v_z - \partial_z v_y\right) + \hat{Y}\left(\partial_z v_x - \partial_x v_z\right) + \hat{Z}\left(\partial_x v_y - \partial_y v_x\right)\right). \quad (5)$$

Substituting equation 4 into 5, we see that on a free surface

$$\begin{aligned} r_x &= \partial_y v_z, \\ r_y &= -\partial_x v_z, \\ r_z &= \frac{1}{2}\left(\partial_x v_y - \partial_y v_x\right), \end{aligned} \quad (6)$$

i.e., the horizontal rotation-rate components can be derived by differencing vertical geophones, and the vertical rotation-rate components can be derived by differencing horizontal geophones.

The challenge with estimating rotations from geophone differencing is the distance required between the adjacent geophones. The upper bound for the distance between the geophones is half the horizontal spatial wavelength, in order to avoid aliasing. The lower bound, however, depends on the level of ambient noise. Differencing the signal of two adjacent geophones necessarily decreases the signal to noise ratio, as we are subtracting most of the actual signal that was recorded on the two geophones. Therefore, since we cannot make a priori assumptions about the frequency and wavenumber of each arrival, we will never be able to acquire rotations reliably for broadband data by geophone differencing alone. We would ideally prefer to not rely on geophone differencing for rotational-data acquisition.

# CONVERSION FROM INDUCTION-COIL MAGNETOMETER RECORDINGS TO ROTATION RATES

## Designature of magnetometer data

Faraday's law states that the voltage $V$ generated within a loop of wire is proportional to the rate of change of the magnetic flux $\Phi$ passing through the loop

$$V = -\frac{d\Phi}{dt}. \quad (7)$$

In an ICM, there are $N$ loops of wire wound around a cylinder of area $A$. The flux can be written as $\Phi = NAB$, where B is the magnetic induction normal to the area of the wire loop

$$V = -NA\frac{dB}{dt}. \quad (8)$$

The magnetic induction $B$ is related to the magnetic field $H$ as $B = \mu_0\mu_r H$, where $\mu_0$ is the magnetic permeability of free space and $\mu_r$ is the relative magnetic permeability of the material that the loop of wire is wound around. The expression for an ICM which includes a permeable core is then

$$V = -NA\mu_0\mu_r \frac{dH(t)}{dt}. \tag{9}$$

Equation 9 shows that the output voltage is linearly related to the number of turns of the wire $N$, the area of the loops $A$ and the relative permeability of the core material in the loop $\mu_r$. The sensitiviy of the the ICM can be controlled by varying these parameters.

Assuming a harmonic time function for the magnetic field $H(t) = H_0 e^{i\omega t}$, the frequency response of an air core ICM is

$$|V| = \omega NA\mu_0 H_0. \tag{10}$$

The air core magnetometer has a voltage sensitivity that is proportional to the frequency. For an ICM with a permeable core, additional boundary conditions of the induced magnetic field in the core are required to derive an accurate instrument response. These conditions have been derived by Key (2003), and are used when designaturing the instrument response of the ICM.

The magnetic data after designature are in the deviation of the magnetic field strength on the 3 orthogonal magnetic components over time:

$$\vec{H}^{\text{dev}}(t) = [H_x^{\text{dev}}(t), H_y^{\text{dev}}(t), H_z^{\text{dev}}(t)]. \tag{11}$$

In order to have the total projection of the Earth's ambient magnetic field on each ICM components, we add the ambient field value using data from the World Magnetic Model (British Geological Survey, 2014) for the location and date when the data were gathered:

$$\vec{H}(t) = [H_x^{\text{dev}}(t) + H_x^{\text{wmm}}(t), H_y^{\text{dev}}(t) + H_y^{\text{wmm}}(t), H_z^{\text{dev}}(t) + H_z^{\text{wmm}}(t)]. \tag{12}$$

## The forward modeling process: Conversion from rotation-sensor data to magnetic vector projections

In order to forward model the magnetic deviations which we would expect to record given rotational data, we use an Euler rotation matrix. The rotation matrix applies 3D rotations to the projections of the ambient magnetic field, as specified by the World Magnetic Model, on each magnetometer component:

$$\begin{bmatrix} H_x \\ H_y \\ H_z \end{bmatrix} = \begin{bmatrix} c(R_y)c(R_z) & -c(R_y)s(R_z) & s(R_y) \\ c(R_x)s(R_z) + c(R_z)s(R_x)s(R_y) & c(R_x)c(R_z) - s(R_x)s(R_y)s(R_z) & -c(R_y)s(R_x) \\ s(R_x)s(R_z) - c(R_x)c(R_z)s(R_y) & c(R_z)s(R_x) + c(R_x)s(R_y)s(R_z) & c(R_x)c(R_y) \end{bmatrix} \begin{bmatrix} H_x^{\text{wmm}} \\ H_y^{\text{wmm}} \\ H_z^{\text{wmm}} \end{bmatrix}, \quad (13)$$

where $c$ and $s$ are cosine and sine, respectively, and $R_{(xyz)}$ are the measured rotations. We subtract the ambient field in order calculate the magnetic deviations we would expect the magnetometers to record given the ground rotations:

$$\vec{H}^{\text{dev}}(t) = [H_x(t) - H_x^{\text{wmm}}(t), H_y(t) - H_y^{\text{wmm}}(t), H_z(t) - H_z^{\text{wmm}}(t)]. \quad (14)$$

## The adjoint process: rotations from magnetic vector projections

Application of equations 7 to 12 provides the values of the projections of a constant vector on our 3 orthogonal components. Our components are rotating in space over time, and therefore the vector's projection on the 3 orthogonal components changes according to the rotations.

The forward modeling process would be to estimate the changes in the vector projection as a function of measured rotations. We consider the calculation of rotations from vector projections to be the adjoint process. In order to calculate the rotations from the projections, we first convert the projection data to the axis-angle representation. The angle of rotation between consecutive time steps is calculated by

$$\theta(t) = \cos^{-1}\left(\frac{\vec{H}(t+\Delta t)\cdot\vec{H}(t)}{\left|\vec{H}(t+\Delta t)\right|\left|\vec{H}(t)\right|}\right), \quad (15)$$

while the unit vector describing the axis of rotation is

$$\hat{u}(t) = \frac{\vec{H}(t)\times\vec{H}(t+\Delta t)}{\left|\vec{H}(t)\times\vec{H}(t+\Delta t)\right|}. \quad (16)$$

Equations 15 and 16 provide the total amount of rotation and the axis of rotation. However, in order to have meaningful rotation data, i.e., comparable to the measurements we would expect from a three-component rotation sensor, we need to convert from the axis-angle representation to the rotation rate around the three orthogonal axes. For that, we must first convert to a quaternion representation of the rotation angle and axis. The interested reader may refer to Hanson (2005) for a comprehensive explanation of the concept of quaternions, as put forth by Hamilton (1844).

Our quaternion four-vector system state $\mathbf{q}$ begins with no rotation, i.e.

$$\mathbf{q}(t=0) = \begin{pmatrix} q_w \\ q_x \\ q_y \\ q_z \end{pmatrix} = \begin{pmatrix} 1 \\ 0 \\ 0 \\ 0 \end{pmatrix}. \tag{17}$$

We use equations 15 and 16 to get the rotation angle $\theta$ and the rotation axis $\vec{u}$, and then we convert to a quaternion representation of the rotation $\mathbf{p}$ with

$$\mathbf{p}(t) = \begin{pmatrix} \cos\frac{\theta(t)}{2} \\ u_x(t) \cdot \sin\frac{\theta(t)}{2} \\ u_y(t) \cdot \sin\frac{\theta(t)}{2} \\ u_z(t) \cdot \sin\frac{\theta(t)}{2} \end{pmatrix}. \tag{18}$$

In order to rotate our system from its state at time $t$ to its new state at time $t + \Delta t$, we need to apply quaternion multiplication ($\star$) of the quaternion $\mathbf{q}$ by $\mathbf{p}$:

$$\mathbf{q}(t+\Delta t) = \mathbf{p}(t+\Delta t) \star \mathbf{q}(t) = \begin{pmatrix} p_w q_w - p_x q_x - p_y q_y - p_z q_z \\ p_w q_x + p_x q_w + p_y q_z - p_z q_y \\ p_w q_y - p_x q_z + p_y q_w + p_z q_x \\ p_w q_z + p_x q_y - p_y q_x + p_z q_w \end{pmatrix}. \tag{19}$$

We can now retrieve the rotations in terms of Euler angles around each axis using the formulation in Diebel (2006):

$$\vec{R}(t) = \begin{pmatrix} \arctan\left(\frac{2q_y q_z + 2q_w q_x}{\left(q_z^2 - q_y^2 - q_x^2 + q_w^2\right)}\right) \\ \text{-arcsin}\left(2\left(q_x q_z - q_w q_y\right)\right) \\ \arctan\left(\frac{2q_x q_y + 2q_w q_z}{q_x^2 + q_w^2 - q_z^2 - q_w^2}\right) \end{pmatrix}, \tag{20}$$

In order to get the rotation rate, we apply a first derivative on the time axis:

$$\vec{r}(t) = \frac{d\vec{R}(t)}{dt}. \tag{21}$$

## The null space of magnetic projections: rotations around the ambient magnetic-field axis

To derive rotations, we rely on the changes of projection of the magnetic field on the three orthogonal ICMs. However, if any part of the rigid-body rotation occurs directly around the magnetic field's axis, no change in projection will occur, and we will effectively be blind to these rotations.

A synthetic example demonstrates this for a scenario where an ICM has sensor antennas in the X, Y and Z directions, and where the ambient magnetic field is constant along the Z axis with a value of 1 Tesla $\vec{H} = (0, 0, 1)$. The solid lines in Figures 5(b), 5(d) and 5(f) are the true rotations applied to the ICM. We use equation 13 to forward model the change in magnetic projections recorded by the three components of the ICM as a result of the rotations. The forward-modeled magnetic projections are shown in Figures 5(a), 5(c) and 5(e). The dashed lines in Figures 5(b), 5(d) and 5(f) are the result of applying the adjoint operation in equations 15 to 21 to the forward-modeled magnetic projections.

In Figure 5(a) we see the change in magnetic projections resulting from a rotation around the X axis $\vec{u} = (1, 0, 0)$. Since the Y antenna is maximally coupled to the field (as $\sin(\theta)$, since it is pointing 90 degrees away from the field), we see a strong response of the Y projection to a rotation around the X axis. There is also a weak change in the Z projection, since the Z antenna is weakly coupled to the ambient field (as $\cos(\theta)$).

In Figure 5(b) we show the rotation rates that were applied to the system in solid lines, and the rotation rates derived from the magnetic projections in dashed lines. The only rotation that occured in this case is around the X axis, and it is recovered correctly.

In Figure 5(c) the rotations are around both the X and Y axes $\vec{u} = (1, 1, 0)$. We see a strong response of the Y projection to a rotation around the X axis, and a strong response of the X projection to the rotation around the Y axis. Again, there is also a weak change in the Z projection. Observing Figure 5(d), we see that both of the rotations around X and around Y were recovered. Note that some rotation occurs around the Z axis as well. This is a result of the coupling between components of 3D rotations: it is not possible to rotate around two axes without causing the third axis to change its attitude in relation to the external frame.

In Figure 5(e) the rotations are the X, Y and Z axes $\vec{u} = (1, 1, 1)$. Observe that there is no difference in phase between Figures 5(e) and 5(c). The rotation around the Z axis does not generate a change in projection of the magnetic field on the ICM components. Consequently, observing Figure 5(f), we see that the rotations around the Z axis were not recovered, as the amplitude is much lower and the phase is wrong.

Both of these effects, amplitude reduction and phase difference, are the result of the null space of the magnetic projections. We cannot recover the amplitude correctly for the rotations occuring around the ambient magnetic field's direction. Additionally, and rather surprisingly, the fact that all other rotations can be recovered correctly generates the phase difference between the induced rotations and the recoverd rotations in Figure 5(f). What we observe are the rotations around Z that are the result of the combined rotations around both X and Y.

The conclusion from Figures 5(a)-5(f) is that if we rely on the Earth's constant ambient magnetic field to record rotations on a three-component ICM, we will likely not recover all rotations accurately. Whether this effect is relevant depends on the

application for which we intend to use the derived rotational data.

## SILVER LAKE SURVEY

We conducted a test survey at Silver Lake, near the town of Baker, California. This is a dry lake bed in the Mojave Desert, where both seismic and magnetic noise are weak enough for our purposes.

We measured rotations using three methods:

1. Three-component inertial rotation sensor: direct measurement of rotations
2. Three-component ICM: measurement of rotations derived from changes in magnetic projections (Equations 7-21)
3. Geophone differencing of adjacent vertical geophones (Equation 6) (Muyzert et al., 2012; Barak et al., 2014).

To acquire these data, we deployed three composite stations comprising the three types of sensors, as shown in Figure 6(a). The 'X' (roll) components of both the ICMs and the rotations sensors were oriented in the inline survey direction, and the 'Y' (pitch) components were oriented in the crossline direction. The 'Z' (yaw) was positive downward. By differencing the two adjacent vertical geophones in the inline direction we can calculate the roll rotational component, and by differencing the two adjacent vertical geophones in the crossline direction we can calculate the pitch rotational component. We cannot, however, obtain the yaw rotational component from the vertical-geophone differencing. For that we would have needed to deploy horizontal geophones as well as vertical geophones.

We had three composite stations, deployed using the pattern shown in Figure 6(b). The spacing between receiver stations was 3 meters, and the shot interval was 5 meters. The inline orientation was toward azimuth $120^o$, while crossline orientation was $30^o$. Magnetic inclination at Silver Lake was $60^o$. Therefore, all components were coupled to the magnetic field similarly.

As a seismic source, we used a Betsy gun. An example of the ignition of one Betsy gun shot is shown in Figure 7(a). The station deployment is shown in Figure 7(b). We used a builder's level to ensure orthogonality between components, and a compass to measure the orientations.

Aside from the three composite stations we used to acquire the active seismic data, we also deployed a remote ICM station (Figure 7(c)), far from the shot locations. The purpose if this receiver was to measure the ambient magnetotelluric noise for later removal from the active-seismic ICM data.

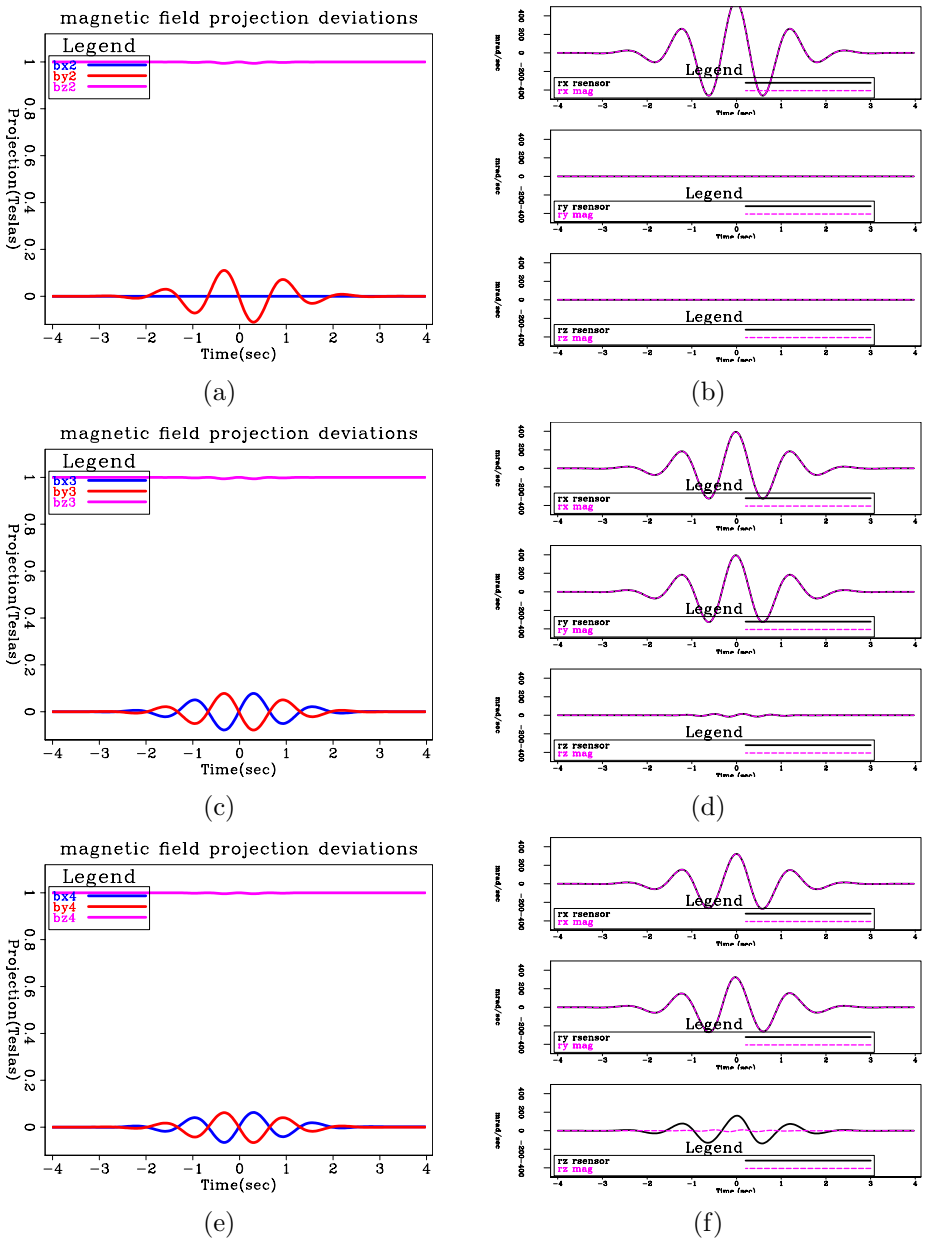


Figure 5: (a), (c) and (e): Changes in magnetic projections on three orthogonal components as a result of rotations of the components within a constant magnetic field $\vec{H} = (0, 0, 1)$ (a vertical magnetic field, as is the case in the Earth's North pole). (b), (d) and (f): The rigid-body rotations (solid lines) that caused the change in magnetic projections, and the rotations derived from the changes in magnetic projections (dashed lines). In (a) and (b), the rotation axis is $\vec{u} = (1, 0, 0)$ (only around the X axis), and the rotation is recovered correctly. In (c) and (d), the rotation axis is $\vec{u} = (1, 1, 0.)$ and the rotations are recovered correctly. In (e) and (f), the rotation axis is $\vec{u} = (1, 1, 1.)$ The rotation around the Z axis (the direction of the magnetic field) is not recovered correctly. Rotations around the magnetic field axis cannot be derived since they do not cause a change in the projections. [**ER**]

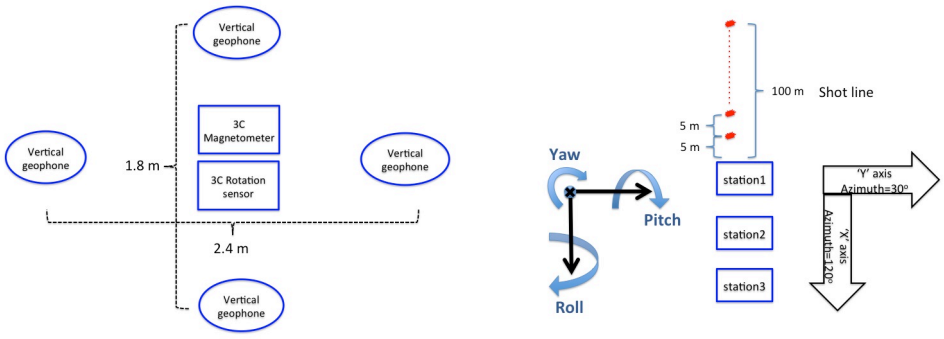


(a) (b)

Figure 6: (a) The arrangement of a single composite station in the Silver Lake survey. Each station had 3 orthogonal ICMs, and a 3C inertial rotations sensor. Two geophones were placed in close proximity in the inline and in the crossline directions. (b) 20 shots were executed off-end, at 5-meter intervals, for a total of 100m of offset. The 'X' (roll) components of the rotation sensors and the ICMs were along the inline direction toward magnetic heading $30^o$. The 'Y' (pitch) components of the rotation sensors and the ICMs were along the crossline direction toward magnetic heading $120^o$. The 'Z' (yaw) components are downward, while magnetic inclination was $60^o$. Note that the figure is not to scale. The distance between the composite stations was 3 meters. [**NR**]

## Detectable rotations

Consider a very simple rotation of the magnetometer axes about the $z$ axis by an angle $\theta$. The magnetic field $\mathbf{H}$ along the sensor axes is then

$$\begin{bmatrix} H_x^{'} \\ H_y^{'} \\ H_z^{'} \end{bmatrix} = \begin{bmatrix} \cos(\theta) & \sin(\theta) & 0 \\ -\sin(\theta) & \cos(\theta) & 0 \\ 0 & 0 & 1 \end{bmatrix} = \begin{bmatrix} H_x \\ H_y \\ H_z \end{bmatrix} \tag{22}$$

For a magnetic field $\vec{H} = (H_0, 0, 0)$, the field in the rotated coordinates will be

$$H_x^{'} = \cos(\theta) H_x, \tag{23}$$
$$H_y^{'} = -\sin(\theta) H_y, \tag{24}$$
$$H_z^{'} = 0. \tag{25}$$

The change in the magnetic field measured by the magnetometers is

$$\Delta H_x = H_x^{'} - H_x = (1 - \cos(\theta)) H_x, \tag{26}$$
$$\Delta H_y = H_y^{'} - H_y = -\sin(\theta) H_y, \tag{27}$$
$$\Delta H_z = 0. \tag{28}$$

(a)

(b)

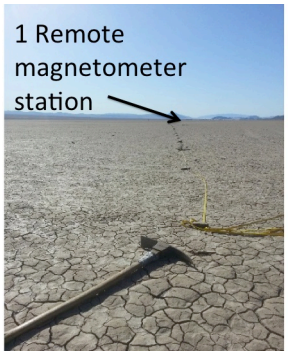


(c)

Figure 7: (a) Execution of one of the 20 shots using the Betsy gun. (b) One of the 3 composite stations. The rotation sensor is housed in the grey box, while the ICMs are the white rods arranged orthogonally. (c) We placed one remote 3-component ICM station far from where we were shooting the seismic data, to record the ambient magnetotelluric noise for later removal in processing. [**NR**]

The table below shows the magnetic field changes for various amounts of rotations assuming a nominal 50,000 nT magnetic field along $x$. This shows that a microradian rotation would produce a pico-Tesla level signal on $H_y$, the maximally coupled orientation direction. Since the MT magnetic field in Silver Lake in the seismic frequency band (1 Hz - 100 Hz) is about $10^{-12}\mathrm{T}/\sqrt{\mathrm{Hz}}$, we can expect to be able to detect rotations down to 1 microradian.

| $\theta$ (rad) | $\lvert 1-\cos(\theta)\rvert$ | $\lvert\sin(\theta)\rvert$ | $5 * 10^{-5}\lvert\sin(\theta)\rvert$ |
|---|---|---|---|
| 1e-09 | 0 | 1e-09 | 5e-14 |
| 1e-08 | 0 | 1e-08 | 5e-13 |
| 1e-07 | 5e-15 | 1e-07 | 5e-12 |
| 1e-06 | 5e-13 | 1e-06 | 5e-11 |
| 1e-05 | 5e-11 | 1e-05 | 5e-10 |
| 1e-04 | 5e-09 | 1e-04 | 5e-09 |
| 1e-03 | 5e-07 | 1e-03 | 5e-08 |
| 1e-02 | 5e-05 | 1e-02 | 5e-07 |
| 1e-01 | 5e-03 | 0.0998 | 4.99e-06 |
| 1 | 0.46 | 0.841 | 4.21-05 |

Since the MT field is expected to be laterally uniform over regional spatial scales, we planned to use the remote station to reduce the MT signal from the local measurement, with the possibility of obtaining MT-free data with a spectrum close to the Ant-6 magnetometer noise floor of $10^{-14}$ to $10^{-13}$ Tesla, as shown in Figure 8. This would give us an equivalent rotational noise floor of about $10^{-9}$ to $10^{-8}$ radians.

## Silver Lake Data: designature of rotation-sensor

According to instrument manufacturer specifications, the rotation sensors have a flat phase response within the frequency band of the data. However, we were unsure whether this was the case for the specific sensors we were using. We knew the instrument response of the geophones however, and used it to designature the vertical geophones. We then used vertical-geophone differencing (Eq. 6) to get an estimate of the designatured rotational pitch signal. We calculated the phase difference between the rotations measured by the rotation sensors and the rotations estimated by geophone differencing. We then used this phase difference as the rotation-sensors' instrument response.

Figure 9(a) shows a receiver gather of the vertical geophone component at station 1. The direct P-wave, propagating at a velocity of 1420 m/s, is much weaker than the ground roll, and is therefore not visible in this section. Two surface wave arrivals are clearly visible, propagating at velocities of 135 m/s and 250 m/s. We interpret these as two modes of a Rayleigh wave generated by the Betsy gun source.

Figure 9(c) is an estimate of the pitch component resulting from differencing the two adjacent vertical geophones in the inline direction (Eq. 6) at station 1 (refer

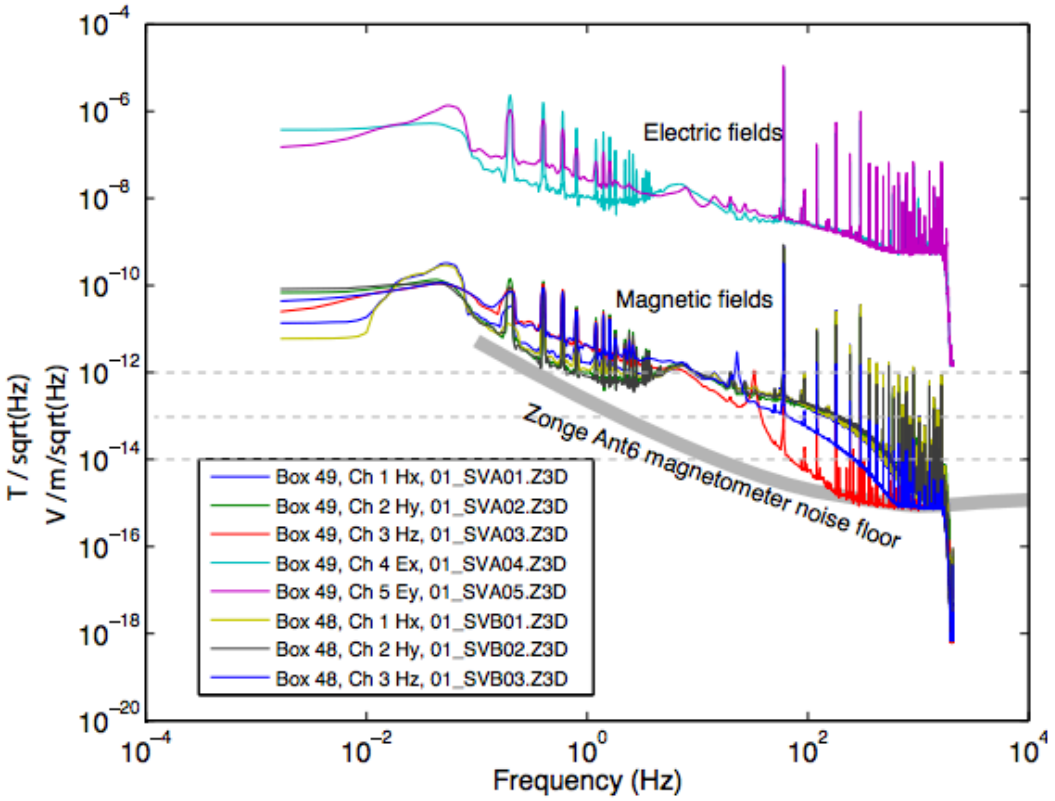


Figure 8: Magnetotelluric magnetic and electric fields observed at Silver Lake, Mojave Desert in March 2015. Also shown is the public-domain noise floor of the Zonge Ant-6 magnetometer. Spikes are from 60 Hz power line noise and 0.2 Hz cathodic protection system on a nearby gas pipeline. [**NR**]

to Figure 6(a)). We compare the data in this figure to the rotation-sensors' pitch component shown in Figure 9(d). Observe that both sections show the same arrivals with similar amplitudes of up to 0.2 mrad/s. However, the weaker Rayleigh-wave arrival appears to have been better acquired by geophone differencing.

We expect the pitch rotational component to be dominant for the Rayleigh wave propagating in the inline direction in this 2D survey, since the rotational deformation that a Rayleigh wave generates is perpendicular to its propagation direction, i.e., rotation around the crossline 'Y' axis.

The phase comparison between the pitch calculated by geophone differencing and the pitch measured by the rotation sensor is shown in Figure 10(a). There seems to be no drastic phase difference between the signals at all 3 stations for the pitch component.

Figure 9(e) is the roll component estimated by differencing the two adjacent vertical geophones in the crossline direction (Eq. 6) at station 1. This figure should be compared the rotation-sensor roll component in Figure 9(f). Note again the similarity in amplitudes. The roll estimated from geophone differencing appears slightly more coherent than the roll from the rotation sensor.

Compared to the pitch component, the roll component is weaker, and appears less coherent. This is again in accordance with the rotational deformation we would expect the Rayleigh wave to generate in this survey, i.e., very little rotation around the inline axis.

Figure 10(b) shows that we are unable to obtain a consistent phase difference between the roll from geophone differencing and the roll from the rotation sensors for the 3 receiver stations. We attribute this to the fact that the roll signal is indeed very weak, therefore discerning the ground-roll signal's phase difference between these two different measurements is difficult.

Figure 9(b) is the yaw component of the rotation sensor at station 1. Note that it exhibits mostly just the strong Rayleigh wave arrival. Like the roll component, it is much weaker than the pitch signal. We cannot compare the rotation-sensor's yaw component to the yaw estimated from geophone differencing, since that would require differencing horizontal geophones which we did not deploy in this survey.

The only reliable phase difference we have is for the pitch component (Figure 10(a)), which does indeed show a flat response for the rotation sensors over the 3-30 Hz frequency range. Though the phase difference is very small, we used it for designature of all rotational components.

## Silver Lake Data: denoising of magnetometer data

In order to reduce the ambient magnetotelluric noise from our magnetometer measurements, we deployed a remote 3C magnetometer station at a distance of about

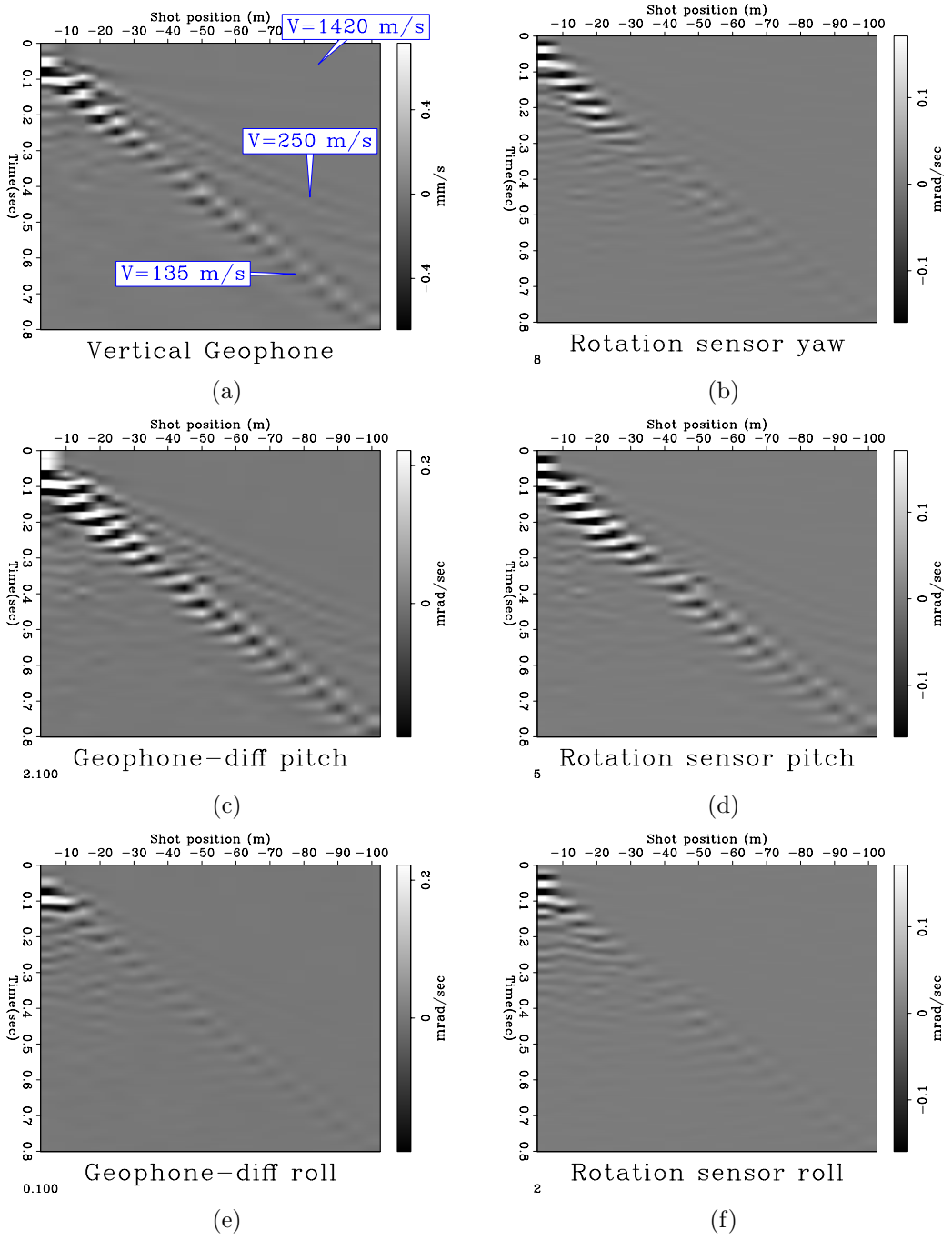


Figure 9: Receiver gathers at station 1, in the 3 - 30 Hz frequency band. (a) Vertical geophone. (b) Yaw rotation sensor. (c) Inline vertical geophone difference, which estimates the pitch component. (d) Pitch rotation sensor. (e) Crossline vertical geophone difference, which estimates the roll component. (f) Roll rotation sensor. The direct wave propagating at V=1420 m/sec is very weak and cannot be seen.. There are two strong Rayleigh wave modes propagating at V=135 m/sec and V=250 m/sec. These are strongly present as rotations measured by geophone-differencing and by the rotations sensors themselves. [**ER**]

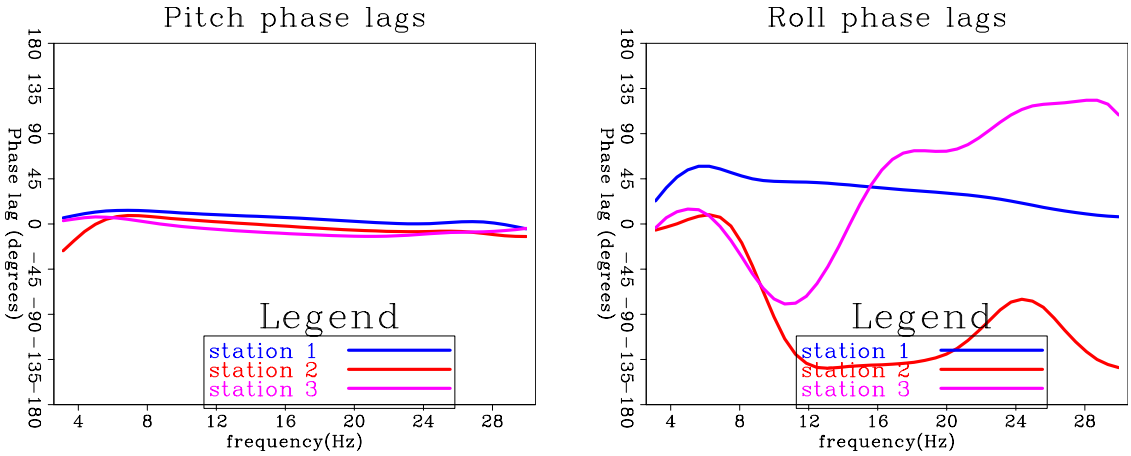


Figure 10: The phase difference between the rotations estimated from vertical geophone differencing and the rotations from the rotation sensors. (a) Phase difference for the pitch component. (b) Phase difference for the roll component. Observe that for the roll we do not get a consistent phase difference for the 3 composite stations. There is not much energy on the roll component, therefore the signal to noise ratio is low and it is difficult to estimate the phase difference reliably for all stations. Also, we could not get an estimation of the yaw component from geophone differencing. Therefore, we designatured the rotation-sensors' pitch, roll and yaw components using the pitch phase difference, which appeared to be reliable across stations. [**ER**]

1 km from our shooting location. The ambient magnetotelluric field varies very little within such a distance. We had intended to use the seismic-free measurements from the remote station in order to subtract the ambient magnetic noise from the active-seismic magnetometers.

Figures 11(a), 11(d) and 11(g) are the magnetometer receiver gather data recorded at station 1. The data are designatured, and therefore are in terms of nanoTeslas of deviation of the projection of the ambient magnetic field on the magnetometer components.

Note that the signal is stronger on the X (inline) and Z (vertical) components, while the Y (crossline) component is the weakest. This is as we would expect given that the Rayleigh wave's rotation is mostly around the Y axis. As a result of a rotation around the Y axis, the X and Z antennas should record a change in projection of the Earth's constant magnetic field.

Figures 11(b), 11(e) and 11(h) are the X, Y and Z magnetometer data recorded at the remote station. These data do not contain any of the magnetic rotation signal generated by the seismic wave, as they are too far away from the shooting location, but they do contain the same magnetotelluric noise as the active seismic magnetometers. Note the similarity between the remote station's and active station's X and Y components before the arrival of the ground-roll.

Note, however, that the vertical magnetometer antenna at this remote station (Figure 11(h)) had an electronic fault, and therefore recorded much more noise than was actually in the field. Consequently, we could not denoise the Z magnetometer component, and were forced to use the original noisy Z magnetometer data in Figure 11(g). This had a deleterious effect on the pitch and roll rotational components derived from the magnetometer data, which is discussed in the following section.

Figures 11(c) and 11(f) are the X and Y magnetometer data at station 1 after subtracting the noise recorded by the remote stations' X and Y magnetometers.

## Silver Lake Data: Conversion from magnetometer deviations to rotations

The pitch rotation is effectively recorded as deviations of the projections of the Earth's magnetic field on the X and Z magnetometers, the roll on the Y and Z magnetometers, and the yaw on the X and Y magnetometers. The changes in projections are on the order of microTeslas. In order to derive rotations from these changes in projections we use equations 7 to 21. We then compare the magnetometer-derived rotations to the rotations-sensor data, which we treat as the "true" seismic rotation data.

Figure 12(a) is the receiver gather of the pitch rotations derived from the magnetometer data at station 1. Compare this with Figure 12(b), which shows the rotations measured by the pitch rotation sensor at the same station. In both figures we observe

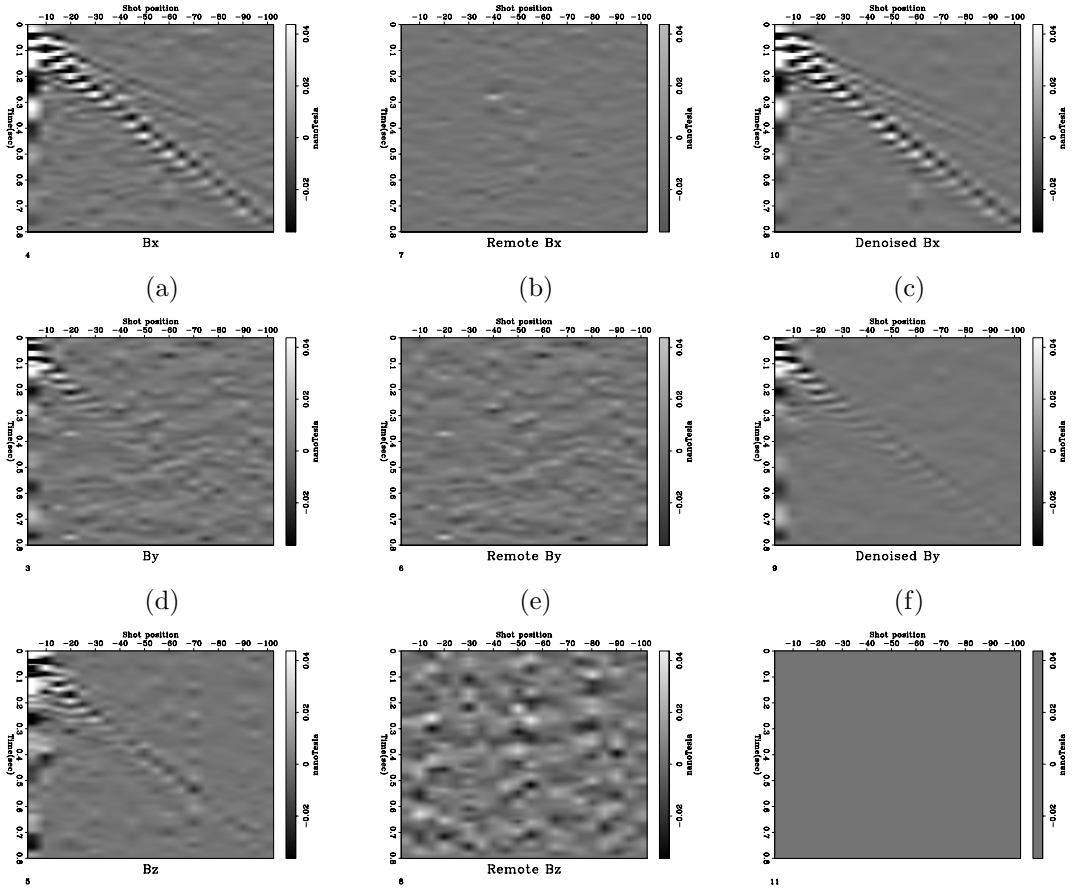


(a) (b) (c)

(d) (e) (f)

(g) (h) (i)

Figure 11: Magnetometer receiver gather at station 1 after designature of the ICMs, before and after removal of the MT field acquired by the remote station. (a) X component before subtraction of MT field acquired by remote station. (b) X component of remote station. (c) X component after subtraction of MT field acquired by remote station. (d) Y component before subtraction of MT field acquired by remote station. (e) Y component of remote station. (f) Y component after subtraction of MT field acquired by remote station. (g) Z component. (h) Z component of remote station. (i) Intentionally blank. Note that we had instrument problems with the Z component of the remote station (h), and therefore we did not subtract the MT noise from the Z component of the three composite stations. [**ER**]

the two strong Rayleigh-wave arrivals. The rotations derived from the magnetometers are slightly weaker. Also, note the higher level of noise in Figure 12(a). This noise is the result of the unattenuated ambient MT noise on the vertical magnetometer, which leaks into the derived pitch rotations.

The most significant difference between these data is the phase of the arrivals. This is more obvious in Figure 13(a), which shows a wiggle-trace comparison of the pitch component resulting from application of the adjoint to the magnetometer data vs the pitch measured by the rotation sensors. Figure 13(b) is the average phase difference between the magnetometer-derived pitch and the rotations-sensor pitch. It shows that within the frequency band of 3 Hz - 30 Hz there is a phase difference between $150^o$ and $90^o$.

The comparison between the magnetometer-derived roll and the rotation-sensor's roll is shown in Figures 12(c) and 12(d). As previously mentioned, we expect the roll component to have the least energy in this survey, and indeed the magnetometer-derived roll is just discernable above the noise. Just as is the case for the magnetometer-derived pitch component, the noise on the magnetometer-derived roll is the result of the ambient MT noise on the vertical magnetometer.

Figure 13(c) shows a wiggle-trace comparison of the roll component at station 1. The noise is more obvious here than in the pitch component section. Figure 13(d) is the average phase difference between the magnetometer-derived roll and rotation-sensor roll. Unlike the pitch component, the phase difference is inconsistent between stations and shows great variability between $90^o$ and $-90^o$. Since the roll signal is weak, the noise is relatively stronger making it more difficult to draw conclusions from the phase differences for this component.

Ideally, we would have crossline shots in the survey which would have generated a strong rotational signal on the roll components. However, time constraints in the field did not enable us to include crossline shots in this survey.

Figures 12(e) and 12(f) compare the magnetometer-derived yaw to the rotation-sensor yaw. Since we were able to remove the ambient MT noise from the X and Y magnetometer antennas, the magnetometer-derived yaw has the least noise of the magnetometer rotations. The earlier, weaker Rayleigh-wave arrival is actually clearer on the magnetometer-derived yaw section than on the rotation-sensor section.

In terms of phase, the difference between the yaw rotations of the magnetometers and that of the rotation sensors is the smallest. Figure 13(f) shows that there is a consistent phase difference of between $90^o$ and $45^o$ between the stations.

## Converting rotations to magnetic projections

By forward-modeling recorded rotations, we can indirectly observe the effect of the null space: the rotations around the ambient magnetic field that would prevent the

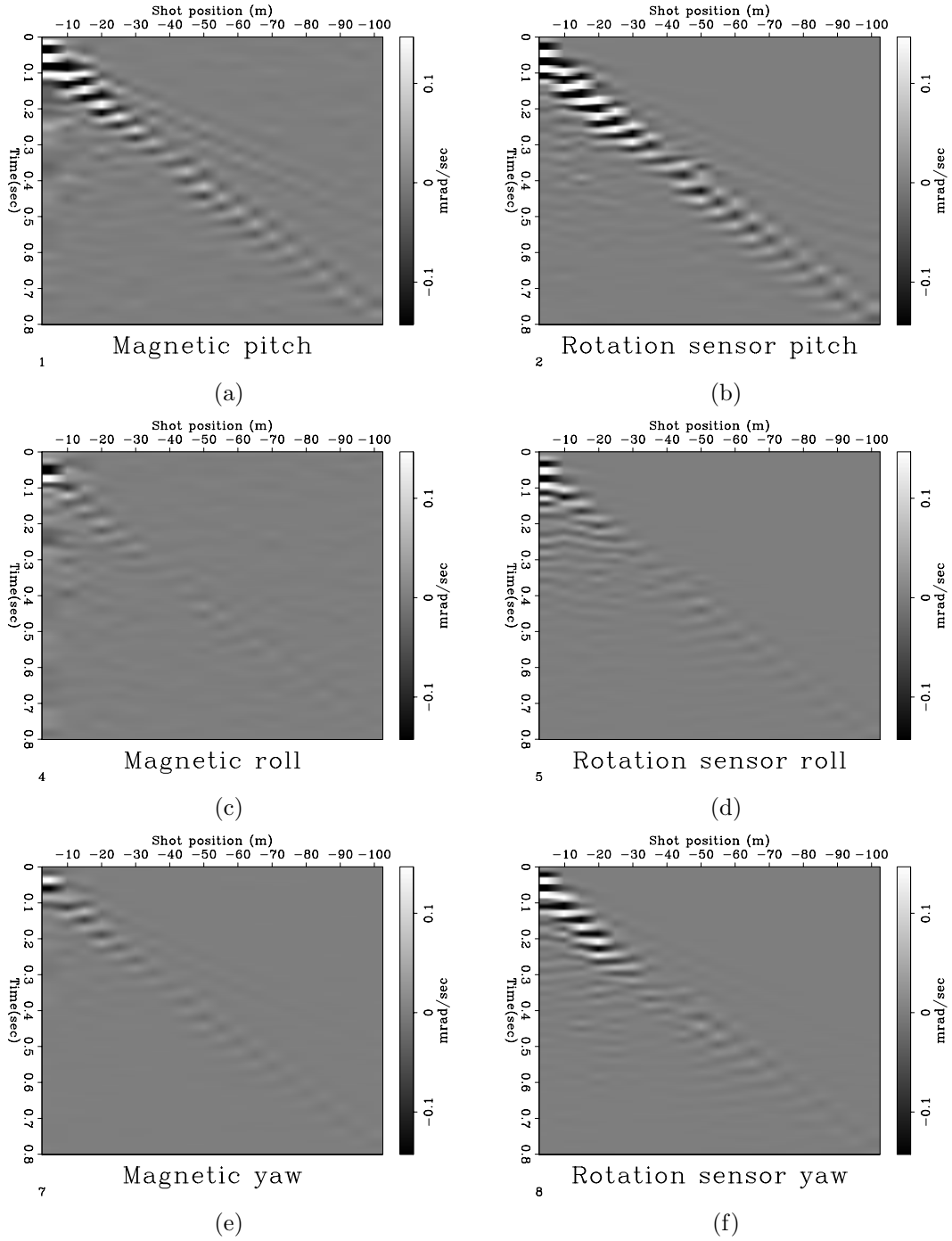


Figure 12: Comparison of rotations derived from ICMs to rotations measured by rotation sensors. (a) Pitch derived from ICM. (b) Pitch measured by rotation sensor. (c) Roll derived from ICM. (d) Roll measured by rotation sensor. (e) Yaw derived from ICM. (f) Yaw measured by rotation sensor. Note the similarity in amplitudes of the Rayleigh-wave arrivals between the magnetometer-derived rotations and those measured by the rotation sensor. Also, note the large phase difference of the pitch component. [**ER**]

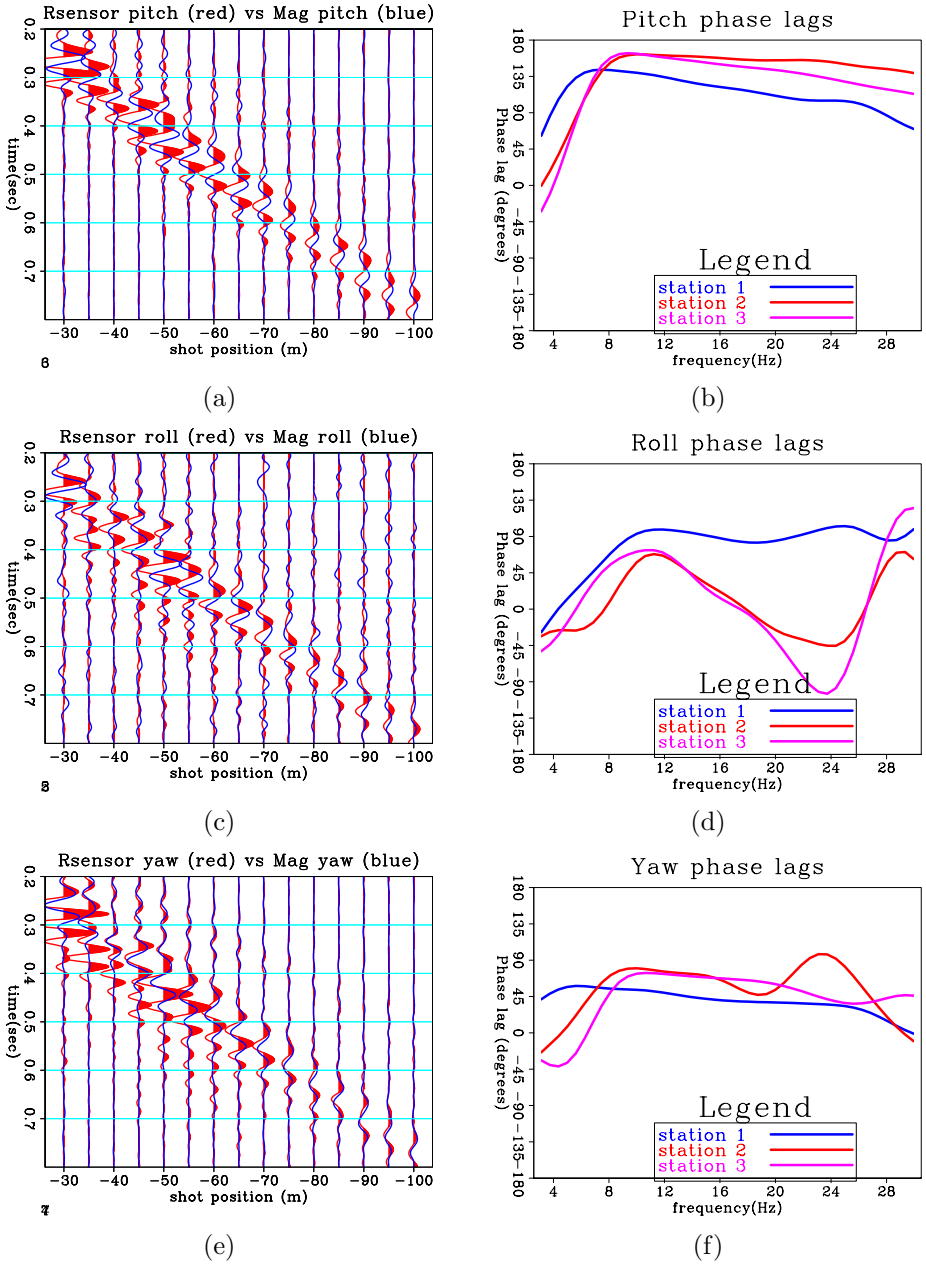


Figure 13: Phase difference between the rotations measured by rotation sensors and rotations derived from ICM components. (a) Comparison of magnetometer-derived pitch with rotation-sensor pitch at station 1. (b) Pitch average phase difference. (c) Comparison of magnetometer-derived roll with rotation-sensor roll at station 1. (d) Roll average phase difference. (e) Comparison of magnetometer-derived yaw with rotation-sensor yaw at station 1. (f) Yaw average phase difference. Trace balancing was applied to each gather separately to enable phase comparison. The roll rotational signal is very weak (see Figure 12(d)), therefore the low signal to noise ratio makes the phase difference unreliable. [**ER**]

recording of those rotations by ICMs. The null-space effect depends on the orthogonality of the rotation and ambient magnetic field axes.

Since we consider the rotational data recorded by the rotational sensors to be the "true" rotations, we apply the forward-modeling operator in equations 13 and 14 to the rotation-sensor data. We compare the forward-modeled magnetometer deviations to the recorded magnetometer data.

Figure 14(a) is the comparison of the forward-modeled 'X' magnetometer component vs the recorded one. We see that the signals are very similar in phase. The 'X' component is derived from the pitch ('Y') and yaw ('Z') rotations. The pitch rotation is the dominant one in the data. Additionally, the 'X' magnetometer component is well-coupled to the field for rotations around the 'Y' axis, as it is nearly orthogonal to the magnetic field. Therefore, the null-space effect is weak on this rotational component, and we indeed observe an agreement between the recorded and the forward-modeled magnetic projections.

Figure 14(c) shows the comparison between the forward-modeled and the recorded 'Y' magnetometer component. We observe an inconsistent phase shift between the signals over offset. The magnetic projection deviations on the 'Y' component are the result of the roll and yaw rotations (around 'X' and 'Z' axes), which are weak in this dataset and therefore have low SNR. Additionally, the 'Y' component is not well coupled (i.e., not orthogonal) to the field for rotations around the 'X' axis. The same reasoning applies to the phase difference we observe for the 'Z' magnetometer component in Figure 14(e).

In conclusion, Figures 14(c) and 14(e) exhibit the effect of the null space on the measurement of rotations with ICMs.

## Silver Lake data: Interpretation of results

Though the results clearly show that both the magnetometers and the rotation sensors are indeed recording seismic energy, the amplitudes and phases of the rotations recorded by the rotation sensors and those derived from the magnetometers are not identical.

The amplitudes of the magnetometer-derived rotations are slightly lower than those of the rotation sensors. We attribute this difference to the rotations around the Earth's ambient magnetic field's axis; the projection null-space effect shown in Figure 5(f). The rotation does not need to be perfectly parallel to the magnetic field's axis in order for the projection's null space to affect the measurements. If the axis of rotation has a projection on the axis of the magnetic field, then invariably some of the resulting magnetic projections will be insensitive to the rotations. The effect of the null space is evident when we compare the forward-modeled magnetic deviations derived from the rotation-sensor data to the recorded magnetic deviations.

In the case of the Silver Lake survey, we had aligned the shot line and receiver

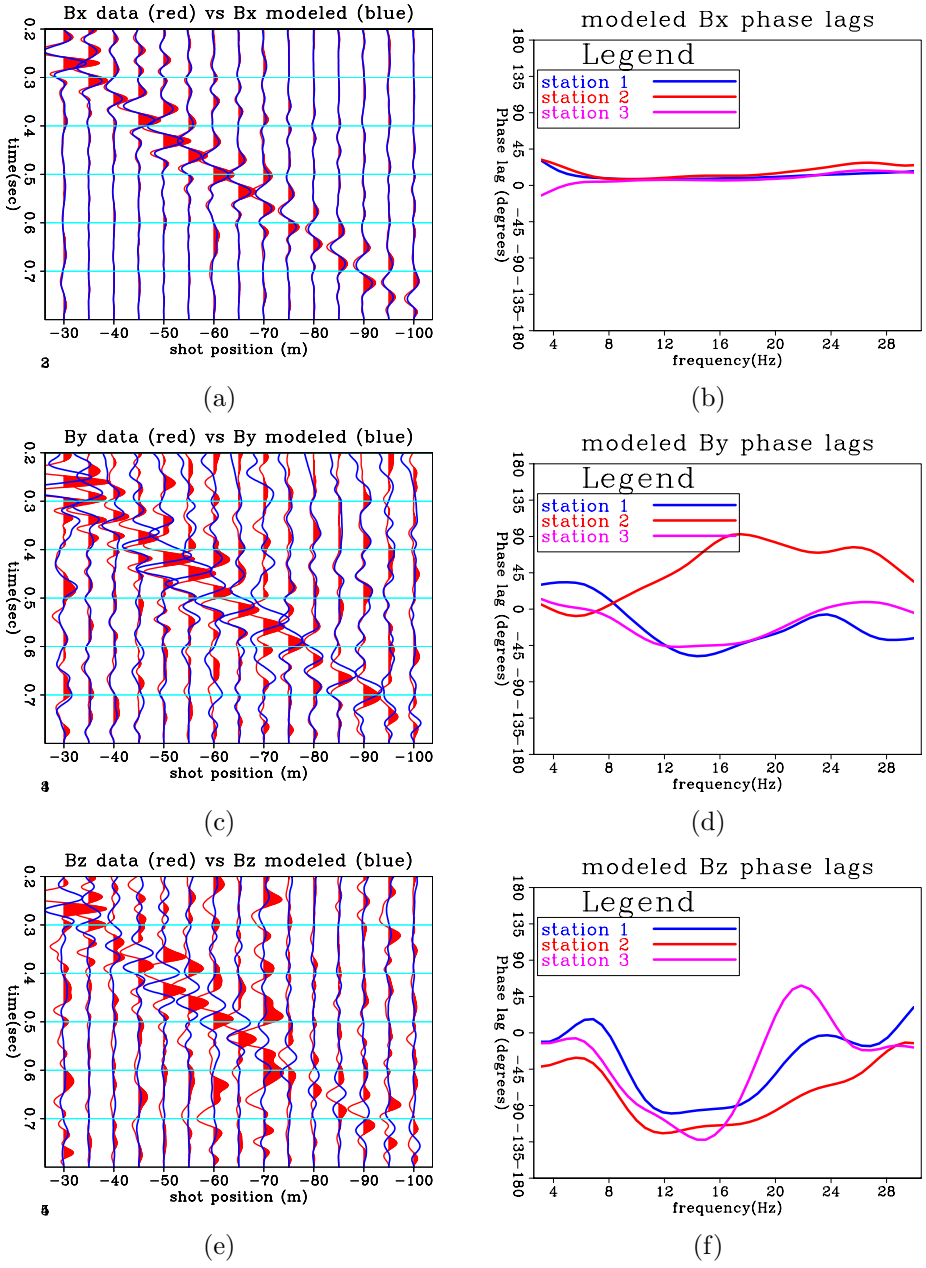


Figure 14: Comparison of the recorded magnetometer data to forward modeled magnetic projections derived from the rotation sensor data. (a) Magnetometer X component (red) vs Magnetic projection X component forward modeled from rotation sensor data at station 1 (blue). (b) Average phase difference. (c) Magnetometer Y component (red) vs Magnetic projection Y component forward modeled from rotation sensor data at station 1 (blue). (d) Average phase difference. (e) Magnetometer Z component (red) vs Magnetic projection Z component forward modeled from rotation sensor data at station 1 (blue). (f) Average phase difference. Trace balancing was applied to each gather separately to enable phase comparison. [**ER**]

components so that the expected axis of the strongest rotation generated by the Rayleigh wave (pitch) would not coincide with the axis of the magnetic field. However, we observe rotations on all components of the seismic rotation sensors, indicating that at least some of the rotations did indeed occur around the magnetic field's axis, leading to a loss of amplitude in the magnetometer-derived rotations.

We attribute the large differences in phase of the pitch component to the null-space issue, since the phase differences appear consistent between receiver stations and along the offset axis. However, the (non-seismic) noise from the vertical magnetometer component necessarily contributed to the rotational signal derived for the perpendicular pitch and the roll components. The case is worse for the roll component, since it has a very low signal to noise ratio to begin with.

We see the smallest phase difference between the two types of rotational measurements for the yaw component. This is partly due to the yaw rotations being well coupled to the magnetic field. It is also due to the yaw component being mostly derived from the magnetic deviations on the X and Y magnetometer components, which we were able to denoise using the remote station's data.

## DISCUSSION AND CONCLUSIONS

In current seismic acquisition, geophones record only the particle velocities but not rotations. Rotations are part of the seismic wavefield, and contain useful information about the seismic energy which can be utilized for a variety of applications.

There are currently very few field-deployable seismic rotation sensors, and none designed for use on the ocean-bottom. Therefore, we presented a methodology for deriving seismic rotations from changes in projection of the Earth's ambient magnetic field on 3-component induction-coil magnetometers. These magnetometers are currently being used for MT and CSEM surveys, are available and are field-deployable in land and marine environments.

The Silver Lake survey shows that, in principle, it is possible to derive rotations from magnetometer data. However, there are limitations to the methodology.

The first challenge is that we must remove the magnetotelluric ambient noise from the ICM data in order to acquire only the magnetic deviations resulting from the seismic energy. In the Silver Lake survey, we used a remote station to record and remove the ambient MT noise from the active-seismic data.

The most critical limitation, however, is the null space of projections: since we are relying on changes in projection of the Earth's ambient magnetic field on the ICM components, any rotation that occurs around the magnetic field's axis will not be recorded. This will cause the derived rotational amplitudes to be lower than the true seismic rotations.

We cannot a priori predict the axis of rotation of seismic waves, therefore the

solution to this problem would not involve a particular orientation of the 3C ICM. Instead, we have considered two possible solutions to the problem.

## Engineering approach

Rather than relying on the Earth's magnetic field, it is possible to generate a strong, local magnetic field (as is already done in CSEM surveys). This local field would be constant in amplitude, but would rotate in a prescribed manner at a frequency much higher than the frequency of the seismic energy. We can then effectively remove the signature of the induced magnetometer current resulting from the local magnetic field's rotation.

Whatever deviations are left in the magnetometer data must then be the result of seismic rotations that rotate the ICM. This method would effectively "smear" the null space effect over the period of measurement, thus reducing the amount of unacquired rotations at any particular time-step. However, this solution entails an additional investment in the logistics and operations of seismic acquisition, which may make it unviable.

## Inversion approach

A possible solution would be to estimate the amount of missing rotational energy by using the collocated 3C geophone data. For example, we expect Rayleigh waves to generate strong rotations. Therefore, if we observe strong Rayleigh waves on the geophone components, but weak Rayleigh waves on the magnetometer-derived rotational components, we may deduce that the axis of rotation is close to that of the ambient magnetic field.

What is required then is a model that provides an expectation of the total rad/sec of rotation for a certain total of mm/sec of particle velocity, for the different types of seismic waves (P, S, surface).

We have a forward operator that maps rotations to magnetic projections. We also have an adjoint operator that maps magnetic projections to rotations. We can therefore invert for the magnetic projections that are in the null space.

The objective function would try to find the model of rotations that match the recorded magnetometer data, and would also have a regularization term that attempts to maximize the rotational amplitudes. The regularization term would be constrained by the amplitudes of the geophone data. The inversion would effectively attempt to recreate the rotations missing from the ICM recording.

## ACKNOWLEDGEMENTS

We thank the sponsors of the Seafloor Electromagnetic Methods Consortium. The rotations sensors used in the field experiment were donated to us by Geokinetics, and we thank John Archer and Patrycjusz Bachleda for preparing the sensors for our use. We also thank Robert Brune for many fruitful discussions. The Silver Lake survey was funded in part by the Mcgee-Levorsen research grant.

## REFERENCES

Barak, O., F. Herkenhoff, R. Dash, P. Jaiswal, J. Giles, S. de Ridder, R. Brune, and S. Ronen, 2014, Six-component seismic land data acquired with geophones and rotation sensors: Wave-mode selectivity by application of multicomponent polarization filtering: The Leading Edge, **33**, 1224–1232.

Barak, O. and S. Ronen, 2016, Wave-mode separation in the complex wavelet domain using combined translational and rotational data : SEP-Report, **163**, 1–19.

British Geological Survey, accessed on May 2014, http://www.geomag.bgs.ac.uk/data_service/models_compass/wmm_calc.html: Online World Magnetic Model Calculator.

Cochard, A., H. Igel, B. Schuberth, W. Suryanto, A. Velikoseltsev, U. Schreiber, J. Wasserman, F. Scherbaum, and D. Vollmer, 2006, Rotational motions in seismology: Theory, observations, simulation: Earthquake Source Asymmetry, Structural Media and Rotation Effects, 391–411.

Diebel, J., 2006, Representing attitude: Euler angles, unit quaternions, and rotation vectors.

Edme, P., E. Muyzert, and E. Kragh, 2014, Efficient land seismic acquisition sampling using rotational data: 76th EAGE Conference and Exhibition, Seismic Noise Attenuation Session, **ELI1 08**.

Hamilton, S. W. R., 1844, On quaternions: or on a new system of imaginaries in algebra: Philosophical Magazine, **XXV**, 10–13.

Hanson, A. J., 2005, Visualizing quaternions: ACM SIGGRAPH 2005 courses, 1.

Kappler, K., N. Cuevas, and J. W. Rector, 2006, Response of induction coil magnetometers to perturbations in orientation: SEG Technical Program Expanded Abstracts, 899–903.

Key, K., 2003, Application of broadband marine magnetotelluric exploration to a 3d salt structure and a fast-spreading ridge: Ph.D. thesis: University of California, San Diego.

Lee, W. H. K., H. Igel, and M. D. Trifunac, 2009, Recent advances in rotational seismology: Seismological Research Letters, **3**, 479–490.

Muyzert, E., A. Kashubin, E. Kragh, and P. Edme, 2012, Land seismic data acquisition using rotation sensors: 74th Conference and Exhibition, EAGE, Extended Abstracts.

Pillet, R., A. Deschamps, D. Legrand, J. Virieux, N. Bethoux, and B. Yates, 2009, In-

terpretation of broadband ocean-bottom seismometer horizontal data seismic background noise: Bulletin of the Seismological Society of America, **99**, 1333–1342.

Vassallo, M., K. Eggenberger, D. J. van Manen, K. Ozdemir, J. Robertsson, and A. Ozbek, 2012, Contributions of the horizontal and vertical components of particle velocity in 3D pressure wavefield reconstruction on dense receiver grids using generalized matching pursuit: SEG Technical Program Expanded Abstracts, 1–5.